



# Investigation on the Controlled Degradation and Invitro Mineralization of Carbon Nanotube Reinforced AZ31 Nanocomposite in Simulated Body Fluid

A. Madhan Kumar<sup>1</sup> · S. Fida Hassan<sup>2</sup> · Ahmad A. Sorour<sup>1,2</sup> · M. Paramsothy<sup>3,4</sup> · M. Gupta<sup>5</sup>

Received: 19 February 2018 / Accepted: 28 June 2018 / Published online: 3 July 2018  
© The Korean Institute of Metals and Materials 2018

## Abstract

Magnesium (Mg) based implant materials are believed to be the perfect candidates for biomedical applications due to their versatile properties. However, regulating their corrosion/degradation rate in the biological surroundings is still a noteworthy task. Suitable strategies to overcome this task is to wisely select alloy elements with improved corrosion resistance and mechanical characteristics. An attempt has been made to enhance the corrosion and biocompatibility performance of magnesium alloy AZ31 containing carbon nanotubes (CNTs) as reinforcement and evaluate its degradation and invitro mineralization performance in physiological medium. Corrosion behavior of AZ31 alloy with CNTs reinforcement was investigated using electrochemical methods, weight loss, and hydrogen evolution in SBF during short and long-term periods. The obtained results revealed that the corrosion resistance of AZ31 alloy enhanced significantly due to the incorporation of CNTs. Hydrogen evolution test and weight loss tests revealed that the presence of CNTs improves the stability of the Mg(OH)<sub>2</sub> and efficiently regulate the degradation behavior in SBF. Surface characterization after immersion in SBF revealed the rapid formation of bone-like apatite layer on the surface, validated a good bioactivity of the AZ31 nanocomposite samples.

**Keywords** AZ31 Mg · CNTs nanocomposite · Corrosion · EIS

## 1 Introduction

The application of magnesium alloys as promising biodegradable orthopaedic implants and subjected to intense research focus in recent years. Significant benefits of

magnesium based alloys over the conventional bio-implants characteristically consist of higher fracture toughness than ceramic biomaterials, greater strength over biodegradable plastics, practically promising elastic modulus and reasonable biocompatibility compared to other metallic implants [1]. In addition, magnesium based implants could dissolve entirely in the physiological medium and their products could be metabolized and absorbed by the human body and hence avoid an additional surgery to remove the implant, which is presently a regular practice [2]. However, the utilization of magnesium alloys as a bio-implant is mainly restricted due to their faster degradation/corrosion rate.

The principle drawbacks of prompt degradation/corrosion comprise of the formation of a high pH and large quantity of hydrogen bubbles on implant surface in initial stages which can harm the nearby tissues. Moreover, the corrosion morphology of magnesium alloys is found to be localized and heterogeneous because of the galvanic potential difference between the alloy matrix and intermetallic phase in the microstructure [3]. This localized corrosion morphology can lead to the early loss of mechanical integrity and hence premature failure before the period

✉ A. Madhan Kumar  
madhankumar@kfupm.edu.sa

✉ S. Fida Hassan  
sfhassan@kfupm.edu.sa

<sup>1</sup> Center of Research Excellence in Corrosion, Research Institute, King Fahd University of Petroleum and Minerals, Dhahran 31261, Kingdom of Saudi Arabia

<sup>2</sup> Department of Mechanical Engineering, King Fahd University of Petroleum and Minerals, Dhahran 31261, Kingdom of Saudi Arabia

<sup>3</sup> School of Science and Technology, Singapore University of Social Sciences (SUSS), Singapore 599491, Singapore

<sup>4</sup> NanoWorld Innovations (NWI), Singapore 368931, Singapore

<sup>5</sup> Department of Mechanical Engineering, National University of Singapore, Singapore 117576, Singapore

necessary for the tissue to become completely cured. Investigations in an exploration of the methods to improve its corrosion resistance are therefore vital and essential for their appropriate arrangement as biodegradable orthopaedic implants [4].

Numerous efforts have been dedicated to delaying the degradation time and improve the bioactivity of Mg alloys [5–7]. Best appropriate strategy for the composition design is to prudently choose reinforcing components in magnesium based composites with improved corrosion resistance and mechanical features. Carbon nanotubes (CNTs) have been deliberated to be perfect reinforcing nano materials for magnesium based composites proposed for biomedical applications owing to their higher surface area with the smaller dimension, better thermal conductivity and good mechanical features [8, 9]. Hence, many attempts have been attained to fabricate Mg metal matrix composites (MMC) with CNTs to advance mechanical performance of several Mg alloys through different routes [10, 11]. Our previous study was performed to make a novel path for manufacturing Mg MMC/CNTs alloy by joining the novel disintegrated melt deposition (DMD) and hot extrusion technique and to elucidate the simple phenomenon that regulate the mechanical performance of the Mg/CNTs MMC [8].

CNTs exhibit prominent capability in the biomedical field, and are utilized in the manufacturing of micro catheters, scaffolds, hard tissue implants and as components for neuronal growth disorders [12, 13]. Further, CNTs deliver added benefit in terms of prompting the formation of hydroxyapatite (HAP) in invitro studies [14]. It has been already reported that the reinforcement of CNTs leads to improvement of the wettability, bonding strength and tensile strength of magnesium matrix composites [15]. Although, there are a few reports about the corrosion behavior of Mg/CNTs samples in 3.5% NaCl solution, an investigation of the existing literature specifies that no successful attempt has been made to investigate the influence of CNTs on the electrochemical corrosion and biocompatibility performance of AZ31 Mg/CNT composites in physiological environment. Hence, for the first time, we explore the controlled degradation/corrosion and invitro mineralization deposition of AZ31 Mg/CNT composites in more detail at physiological environment and in a prolonged time, from start of corrosion until extended duration of 14 days. By combining the electrochemical and surface characterization techniques, we also deliver more understanding of the role of CNTs during Mg corrosion and apatite deposition during immersion in simulated body fluid.

## 2 Experimental Procedures

### 2.1 Materials

The material studied in this study was a disintegrated melt deposition (DMD) processed extruded AZ31 nanocomposite. The reinforcement used was of 1% multiwall carbon nanotubes (CNTs). Details of the processing method and properties of the developed nanocomposite are available in our earlier publication [8]. Though this alloy has aluminum, it has been suggested that the AZ31 alloy, comprises a tolerable quantity of Al believed to be acceptable for use in the human body. Cylindrical extruded nanocomposite samples (with a diameter of 8 mm and height of 10 mm) were prepared by linear cutting, mounted in epoxy. And then, the samples were polished using silicon carbide emery paper with a grit size from 400 to 2400, and subsequently rinsed with deionized water followed by ultrasonication using acetone, dried in an air earlier to experiments. Processing and preparation of unreinforced AZ31 were done following same steps to be used as reference material for comparison.

### 2.2 Electrochemical Studies

Electrochemical and invitro biocompatibility measurements were performed in SBF. Electrochemical measurements were carried out on Gamry electrochemical workstation with a three-electrode setup comprising the CNT reinforced AZ31 nanocomposite as working electrode with an exposure area of  $0.505 \text{ cm}^2$ , a graphite bar and saturated calomel electrode (SCE) as auxiliary and reference electrodes respectively. Electrochemical impedance spectroscopic (EIS) measurements were performed at open circuit potential (OCP) with the scan frequencies ranged between 100 kHz and 0.01 Hz, and with an amplitude of 10 mV. Linear polarization resistance (LPR) were carried out between  $-20$  and  $+20$  mV against the  $E_{\text{corr}}$  with the scanning rate of 0.125 mV/s. Potentiodynamic polarization plots were attained in the potential region of  $E_{\text{ocp}} \pm 250$  mV with a scan rate of 0.5 mV/s. All of the electrochemical corrosion tests were reiterated at least three times and are reproducible. All the tests were carried on unreinforced AZ31 alloy for comparison purpose.

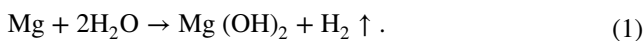
### 2.3 Structural and Surface Characterization After Immersion

Invitro mineralization on unreinforced and CNT reinforced AZ31 samples were analyzed through the various surface and structural characterizations after exposed to SBF medium in different time periods. X-ray diffraction pattern

was obtained using X-ray diffractor (Rigaku Corporation, Tokyo, Japan) with the scattering angle region of  $20^{\circ}$ – $80^{\circ}$  at a  $2\theta$  step of  $0.02^{\circ}$ . ATR-IR spectra of the magnesium alloys were monitored in the region of  $400$ – $4000\text{ cm}^{-1}$  using IR reflectance spectrophotometry (Thermo scientific, with universal ATR attachment with a diamond and ZnSe crystal). Field emission scanning electron microscope (FE-SEM, Tescan Lyra-3) with the associated energy dispersive X-ray analyser (EDS), was employed to examine the morphological, surface elemental composition and microstructural attributes of the bare and nanocomposite samples after immersion.

## 2.4 Degradation Rate Measurement

Hydrogen evolution reaction and resulting degradation behavior were observed during the immersion of unreinforced and reinforced AZ31 alloy samples in SBF. The degradation rates after the exposure of SBF for about 336 h were assessed through weight loss and hydrogen evolution process. Figure 1 shows the hydrogen evolution technique, where the hydrogen evolution volume was monitored, and the degradation rate was assumed from the reaction under:



In the weight loss technique, the exposed samples were separated from the SBF after soaking, washed with distilled water, and dried. Further, the samples were then dipped in chromate acid for about 5–10 min to eliminate the corrosive layer. Subsequently, the samples were cleaned with distilled water and dried again. The dried samples were weighed,

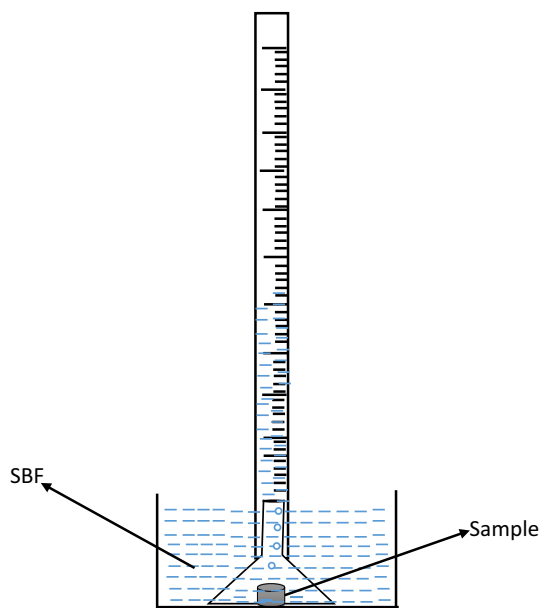


Fig. 1 Schematic representation of hydrogen evolution experiments

and the corrosion/degradation rate was estimated using the representation below:

$$\text{DR} = \Delta m / A t \quad (2)$$

where DR denotes to the degradation rate,  $\Delta m$  represents the weight loss during the exposure time, and A and t denote the exposed area and time in SBF, respectively.

## 3 Results and Discussions

### 3.1 Electrochemical Corrosion Behavior in SBF

Linear polarization resistance (LPR) is measured by plotting potential versus current, and further estimated by curve fitting method as shown in Fig. 2 for CNT reinforced nanocomposite and unreinforced AZ31 samples with different immersion time. In general, increase in the value of LPR reveal high corrosion resistant of the material [16]. LPR values of unreinforced and nanocomposite samples (Fig. 3a) were increased with increasing the immersion time from 10 min to 2 h and afterward, the LPR values of the unreinforced AZ31 alloy were reduced with increasing the immersion time till 336 h. However, LPR values of nanocomposites increased till 72 h and then slightly decreases and remained constant value of about  $600\ \Omega\ \text{cm}^2$  at 336 h.

Figure 3b displays the  $i_{\text{corr}}$  values of unreinforced and reinforced AZ31 nanocomposite samples with different immersion time up to 336 h. Corrosion current density of AZ31 alloy, irrespective of reinforcement status, decreased with increasing the immersion time up to 2 h (Fig. 3b). Besides, the  $i_{\text{corr}}$  values of unreinforced increased after 24 h and promptly raised up to 336 h and reached the value of  $180\ \mu\text{A}\ \text{cm}^{-2}$ . This results indicated that the unreinforced samples formed the corrosion product layer ( $\text{Mg}(\text{OH})_2$ ) till 24 h, which was broken down due to the attack of aggressive species ( $\text{Cl}^-$ ) from electrolyte [17]. However,  $i_{\text{corr}}$  values of CNT reinforced AZ31 nanocomposite samples slightly increased with increasing immersion time up to 72 h and gradually reduced and reached a steady value after 120 h. The obtained results revealed that the addition of CNTs as reinforcement into AZ31 matrix improves the stability of  $\text{Mg}(\text{OH})_2$  layer and thereby increasing the corrosion resistant behavior in SBF medium.

Potentiodynamic polarization curves of unreinforced AZ31 alloy and its CNT reinforced nanocomposite samples in SBF are given in Fig. 4a, b. Electrochemical corrosion kinetic factors such as corrosion potential ( $E_{\text{corr}}$ ), corrosion current density ( $i_{\text{corr}}$ ), and corrosion rate are listed in Table 1. Both the unreinforced and reinforced nanocomposite samples revealed active corrosion performance by exhibiting the increase of the anodic current with increasing potential, signifying that a passive layer was not formed

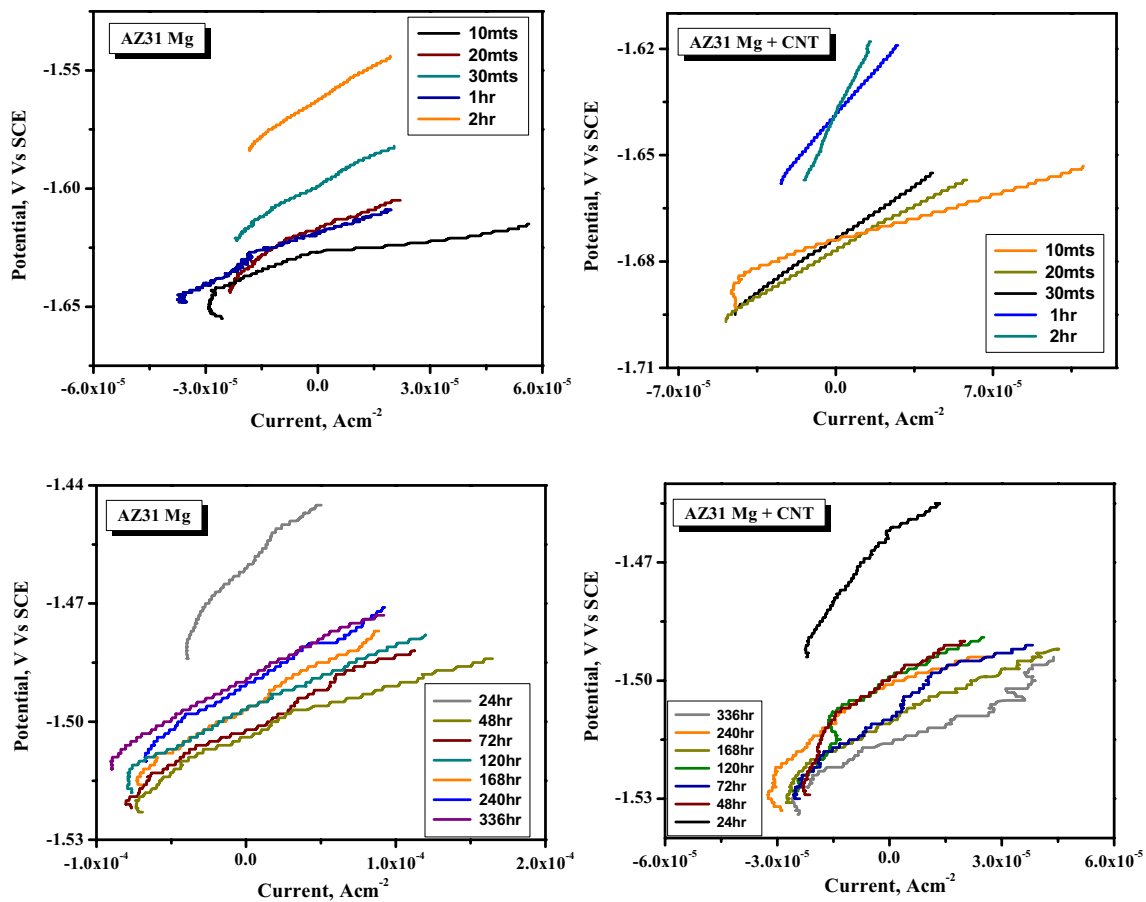


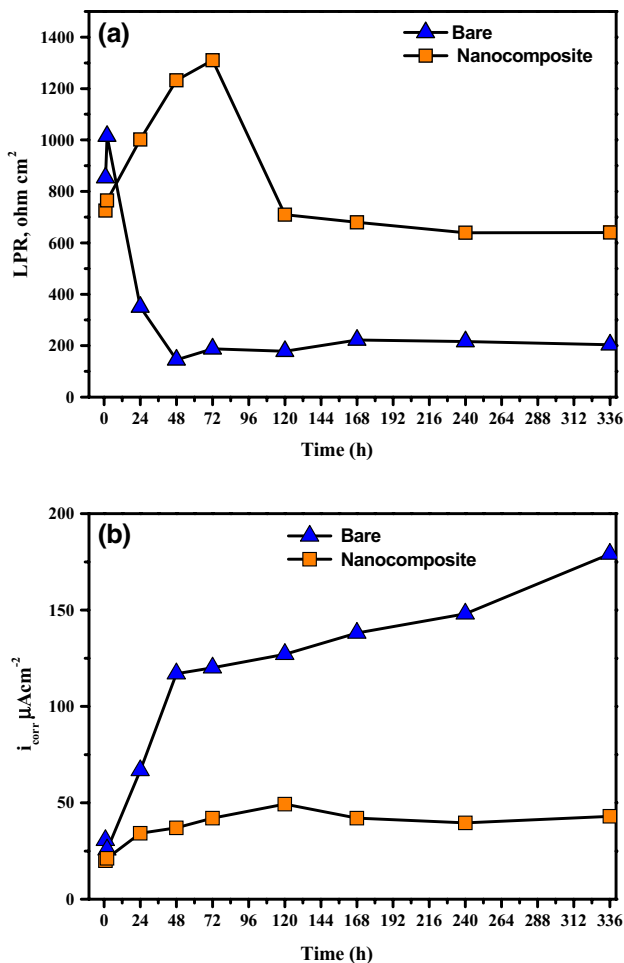
**Fig. 2** LPR results for unreinforced AZ31 and its reinforced nanocomposite samples in SBF medium for short and long immersions

over the alloy surfaces in SBF. In general, the anodic and cathodic branches at polarization curves characterize dissolution of the investigated samples and hydrogen evolution process, respectively. Among the anodic regions in different exposure time, linear Tafel area did not occur in the concentrated polarization area due to the negative difference effect of Mg. This unusual performance of Mg in which hydrogen evolution is dominant over the anodic polarization [18, 19]. As the anodic and cathodic regions were asymmetrical, the corrosion potential ( $E_{\text{corr}}$ ) and corrosion current density ( $i_{\text{corr}}$ ) values were extracted using Tafel extrapolation of the cathodic polarization curve.

Comparing the polarization curves of the unreinforced and nanocomposite samples, it can be stated that the shape of the curves was similar with variation in the corrosion parameters. In general, a high  $E_{\text{corr}}$  and low  $i_{\text{corr}}$  specify good corrosion resistance performance of material. From Table 1 it was clearly understood that nanocomposite samples exhibit the noblest  $E_{\text{corr}}$  after immersion in 336 h, which implies its higher corrosion resistant compared to the unreinforced counterpart. Besides, it also exhibited the lowest corrosion rate in terms of  $i_{\text{corr}}$  compared to the unreinforced

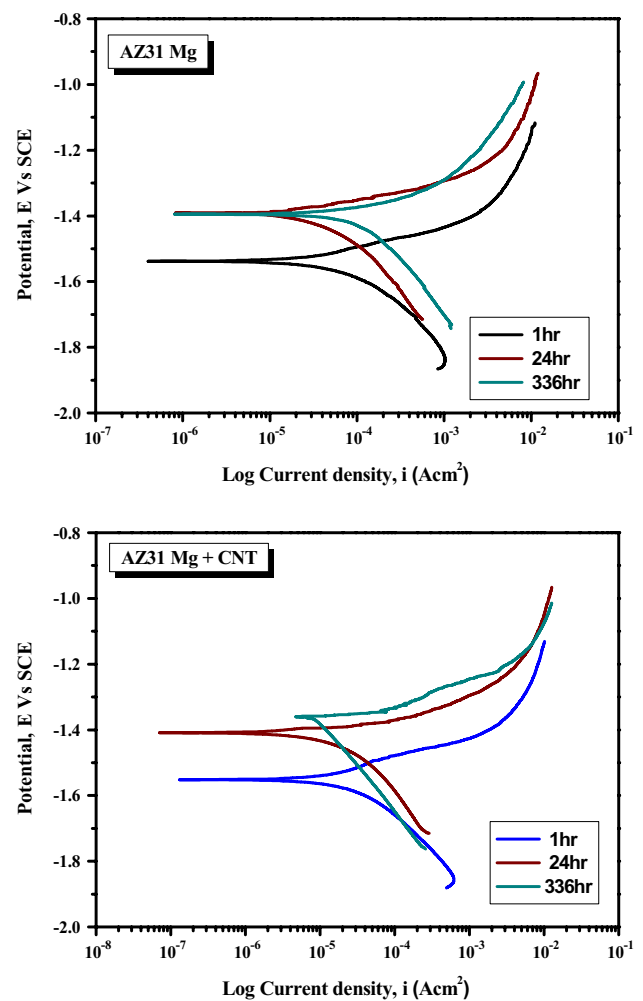
alloy. The magnitude of  $i_{\text{corr}}$  is generally utilized to explain the electrochemical corrosion reaction rate based on the corrosion dynamics. It was evident from the results that the  $i_{\text{corr}}$  slowly increased with increasing of the immersion time before 24 h, after 24 h, the value decreased, which could be attributed to the gradual accumulation of corrosion products on nanocomposite samples surface forming the barrier to slow down the further corrosion.

Figure 5 shows the EIS results of unreinforced and reinforced AZ31 alloy in the form of Nyquist and Bode graphs for short immersion times up to 2 h in SBF medium. Nyquist diagram specifies the appearance of two capacitive arcs at high and medium frequency range with an inductive loop at low frequency range, leading to three time constants, which characterize three different interfacial phenomenon. The achieved results are in good consistent with the previous studies for the magnesium based alloys [20, 21]. The large capacity arcs of the Nyquist graphs at high frequency region was related to the characteristics of the electric double layer located at the interface of electrode/electrolyte, whereas the small capacity arcs at medium frequencies display the features of the corrosion products. The induction response



**Fig. 3** a LPR and b  $i_{corr}$  values of unreinforced AZ31 and its reinforced nanocomposite samples in SBF medium

observed at low frequencies designate localized/pitting corrosion and damage to the corrosion product layers [22]. Equivalent circuits (Fig. 5) were utilized to fit the obtained EIS curves and infer the factors of the circuit components, which further illustrate the corrosion evolution at the interfaces. These factors of the circuit components can offer an enhanced understanding of the complete corrosion performance of the investigated samples.  $R_s$  and  $R_1$  denote the electrolytic and the charge transfer resistance, respectively. Constant phase elements CPE1 and CPE2 were employed on behalf of capacitance to compensate the deviance of heterogeneity from a perfect capacitance. A CPE1 signifies the electric double layer capacitance at high frequency region and CPE2 denotes the capacitance at medium frequency region of the corrosion products.  $R_2$  signifies the resistance of the corrosion products. Inductance component  $L$  is utilized to designate the inductance loop at low frequency region, produced by localized/pitting corrosion, defect-induced corrosion and failure of the films of corrosion



**Fig. 4** Potentiodynamic polarization results for unreinforced AZ31 and its reinforced nanocomposite samples in SBF medium in different immersion periods

products.  $R_L$  characterizes the inductance resistances of the inductance component [23]. In general, the diameter of the capacitive arc in Nyquist plots is inversely proportionate to the corrosion rate, i.e., the larger the diameter, the lesser the corrosion rate [24]. Nyquist diagrams of the unreinforced AZ31 exhibited an increase in the size of the capacitive loop related to higher resistance with the increasing of exposure time from 10 min to 2 h, which can be attributed to the accumulation of corrosion product on the alloy surface. However, the size of the inductive loop also increases with the time, demonstrating severe localized/pitting corrosion of the magnesium alloy for long immersion time [22]. Nanocomposite samples exhibited the improved corrosion resistant behavior compared to the unreinforced alloy by presenting the highest  $R_1$ ,  $R_2$  and significantly lower capacitive loop with long immersion time.

In the short immersion time, the maximum phase angle in Bode plot of unreinforced and reinforced AZ31

**Table 1** Potentiodynamic polarization parameters for unreinforced AZ31 and its reinforced nanocomposite samples after immersion in SBF medium

Samples	Duration (h)	$E_{\text{corr}}$ mV	$I_{\text{corr}}$ A cm $\times 10^{-5}$	$\beta_a$ mV/dec	$\beta_b$ mV/dec	Corr. Rate (mm/year)
AZ31 Mg	1	-1.545	9.470	95	85	2.176
	24	-1.441	4.422	64	78	1.016
	336	-1.402	21.345	96	67	4.906
AZ31 Mg+ CNT	1	-1.502	8.762	83	75	2.013
	24	-1.408	1.742	64	83	0.400
	336	-1.373	0.933	72	91	0.214

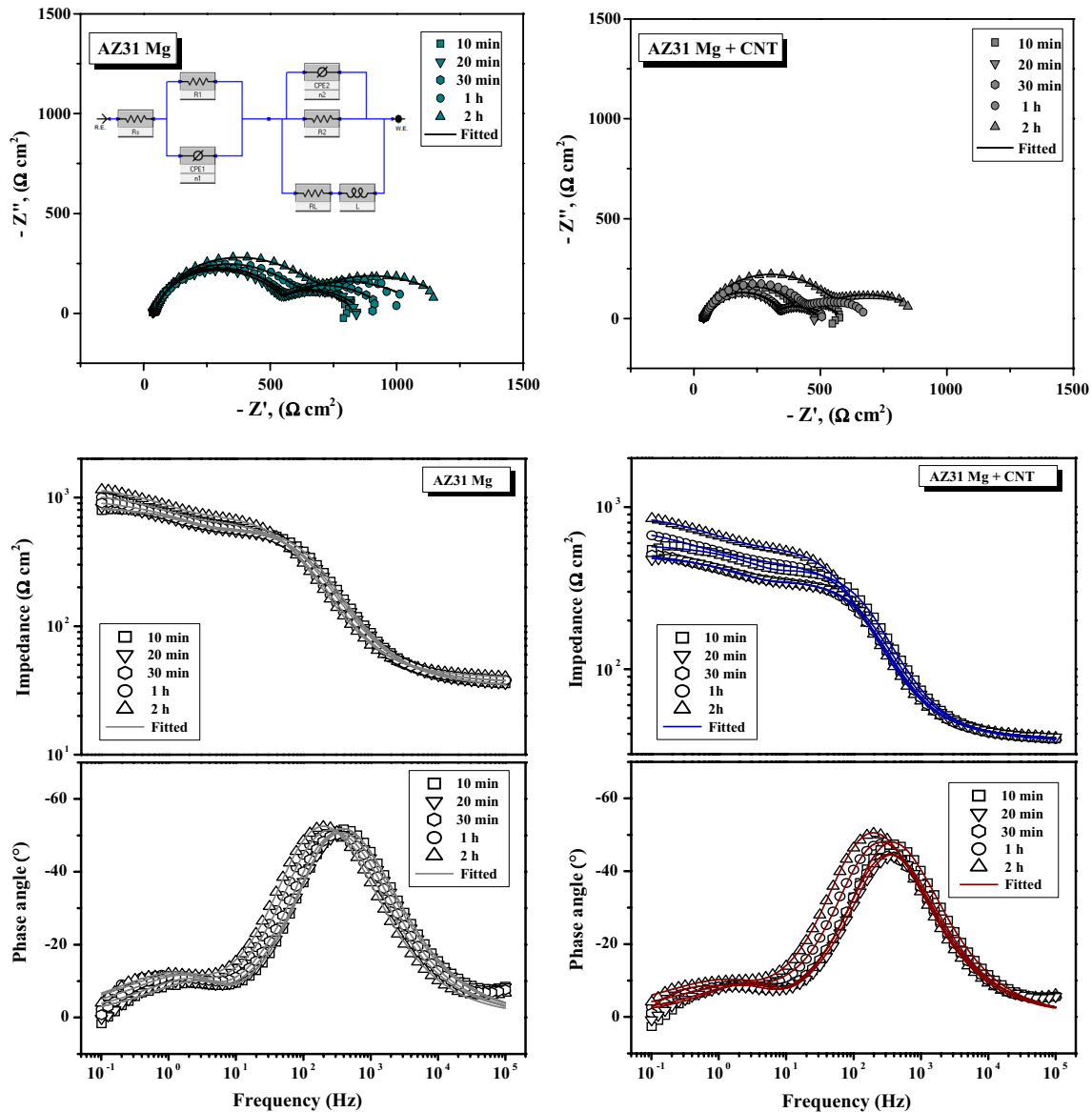


**Fig. 5** EIS results for unreinforced AZ31 and its reinforced nanocomposite samples in SBF medium in short term immersion

nanocomposite samples obtained around 1 kHz in initial 10 min. In which the maximum phase angle was shifted to lower frequency region with increasing the immersion time,

indicating the delayed dissolution of the matrix material. This behavior was occurred due to the formation of magnesium oxide/hydroxide film over the AZ31 alloy surface,

which thickened gradually with immersion time up to 24 h [20]. Furthermore, the maximum phase angle increases from about  $-55^\circ$  to  $-45^\circ$ , which means the oxide/hydroxide layer was permeable and imperfect because of the accumulated loose corrosion product, though this film was thickened with extended immersion time.

EIS spectra of unreinforced AZ31 alloy and nanocomposite samples obtained in immersion periods up to 336 h is shown in Fig. 6. In general, impedance value at low frequency play the major role to explain the corrosion resistant characteristics of alloy samples. Herein, the impedance value of unreinforced AZ31 alloy at low frequency was gradually increased till the immersion time of 24 h, which could be related to the production of a corrosion product

film with improving surface protection with time. Conversely, an opposite trend was observed with prolonged immersion periods, which was the resultant of increased corrosion rate owing to the breakdown of the corrosion protective film and as well the occurrence of a localized/pitting corrosion. It has already been reported that the impedance values of AZ91 alloy samples in a physiological environment decreased with the prolonged exposure time and observed only one capacitive arc, which was due to the presence of severing localized/pitting corrosion [25]. The significant difference in the degree of the three time constants designates the happening of different corrosion stages with a fluctuating corrosion mechanism.

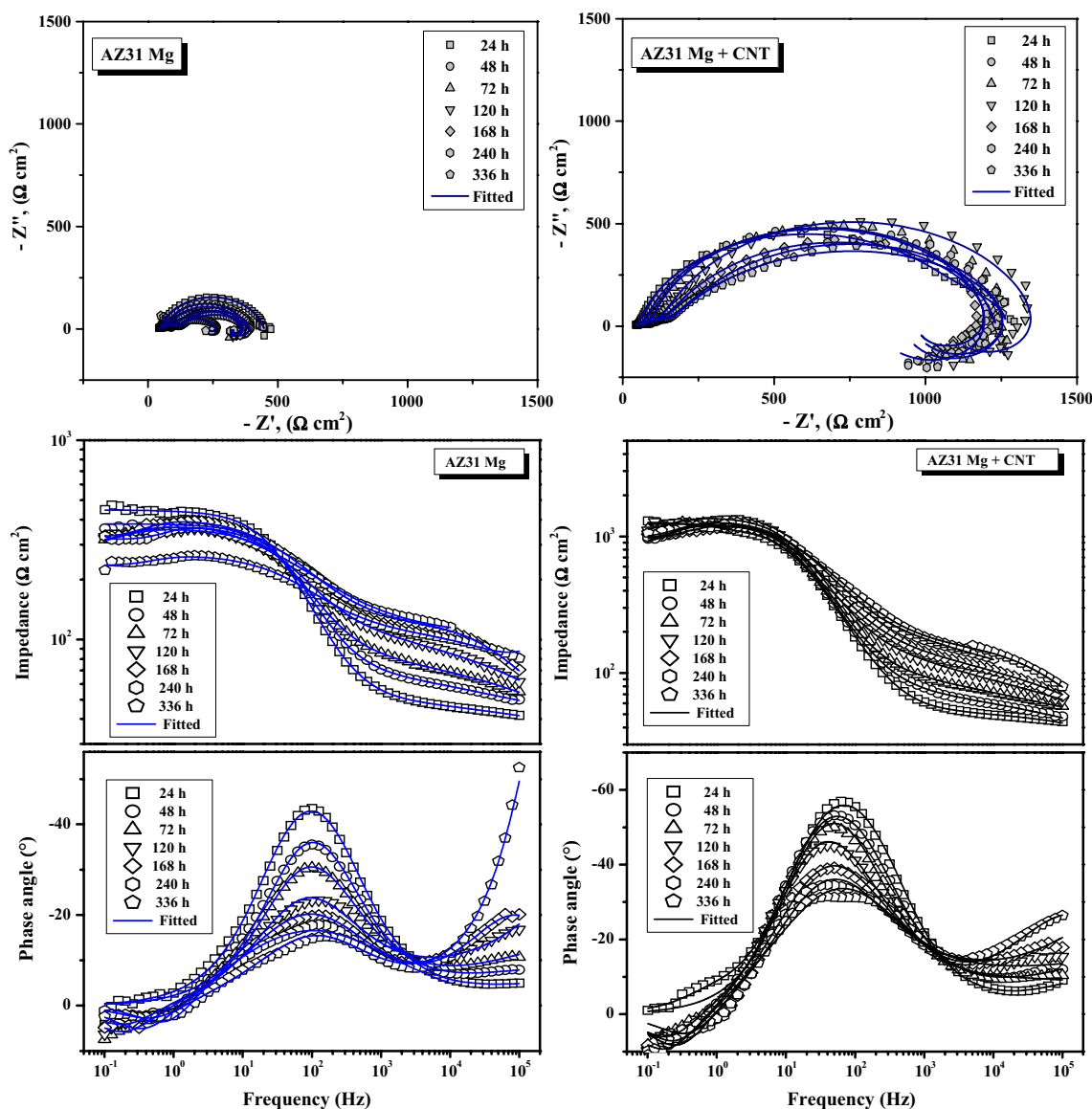
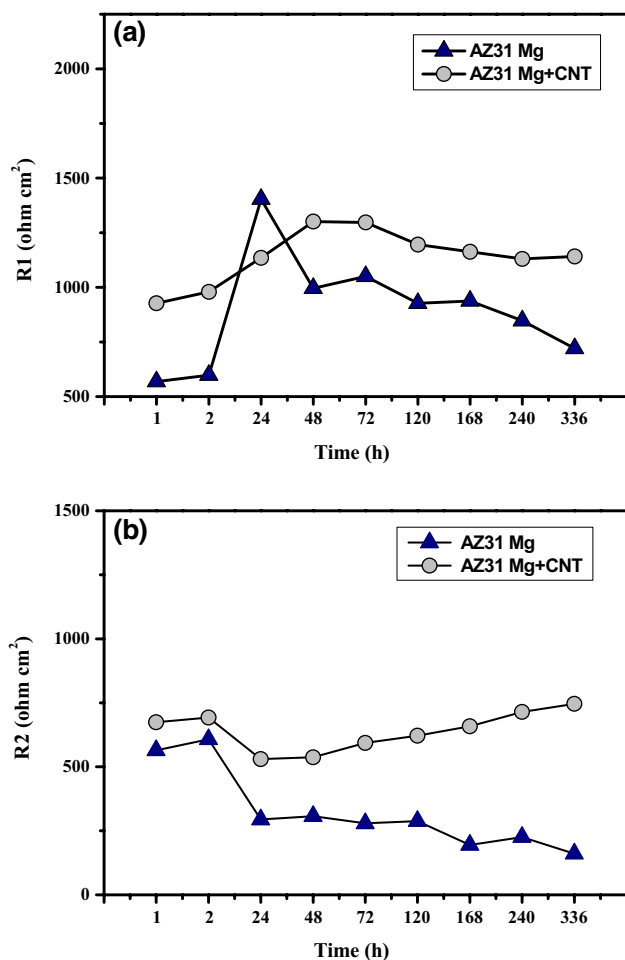


Fig. 6 EIS results for unreinforced AZ31 and its reinforced nanocomposite samples in SBF medium in long term immersion

It is evident from Fig. 6 that the impedance value of the reinforced nanocomposite samples at the low frequencies increases at an initial stage of 120 h of immersion and then gradually decreases and remained constant value of  $1.2 \times 10^3 \Omega \text{ cm}^2$ . However, the unreinforced samples exhibited the prompt decrease from 24 h to throughout the immersion time and remained the low value of  $250 \Omega \text{ cm}^2$ , which reveal the severe corrosion attack due to aggressive species from the electrolyte.  $R_1$  and  $R_2$  values of unreinforced and nanocomposite substrates with the function of time are shown in Fig. 7. Both the values (i.e.,  $R_1$  and  $R_2$ ) of unreinforced alloy decreases with increasing exposure time, which revealed the severe localized/corrosion on the alloy surface with extended immersion time. However, the nanocomposite samples showed an initial increase in the value of charge transfer resistance ( $R_1$ ), achieved for about  $1300 \Omega \text{ cm}^2$  around an immersion time of 48 h and subsequently increasing gradually till 72 h.



**Fig. 7** Charge transfer and diffusion resistance values for unreinforced AZ31 and its reinforced nanocomposite samples in SBF medium

The initial increase in  $R_1$  could be accompanied by the production of a stable corrosion layer with the inclusion of CNTs as a reinforcement which apparently improved surface protective performances. On the other hand, gradual decreasing the value of  $R_1$  after 120 h could be due to the rupture of the corrosion protective film and could be due to the presence of pores and cracks through which the metallic surfaces exposed to the corrosive ions from the electrolyte in longer exposure time [26]. In the case of diffusion resistance ( $R_2$ ), it continued to be low during the initial 24 h, then a linear increase obtained and reached a maximum value of about  $730 \Omega \text{ cm}^2$  at 120 h. Further, it reached an almost constant value after 336 h. The  $R_2$  behavior designates the formation of a partially protecting corrosion film with low diffusion resistance during the initial 24 h of exposure time, followed by a slightly increase in the diffusion resistance, possibly because of the production of a more compact corrosion layer with the inclusion of CNTs. In the case of unreinforced AZ31 alloy, the reduction in the value of diffusion resistance ( $R_2$ ) after 24 h could be accompanied with the partial rupture of the corrosion film influenced by attack of  $\text{Cl}^-$  ions, while the pseudo constant  $R_2$  value after 120 h implies the existence of a non-protective corrosion film, possibly because of the much severe localized corrosion [27]. From the comparison of unreinforced and reinforced samples,  $R_1$  and  $R_2$  values were higher in the case of nanocomposite which further confirmed the enhanced corrosion resistant behavior in SBF medium. Mindivan et al. evaluated the corrosion performance of Mg MMCs with two different amounts of CNTs and showed pointedly enhanced corrosion performance with small CNT contents (0.5%). The obtained results also inferred that the large amounts of CNTs (4%) increased the corrosion rate due to the existence of interfaces between chip layers breaking the stability of the Mg matrix and making favored locations for corrosion attack [28]. Endo et al. reported that the corrosion resistance of AZ91D Mg/CNTs MMC was improved in comparison with the unreinforced AZ91D [29] and it was also revealed that CNTs perform as a water repellent and strengthen the surface protective film against corrosion. In contrast, Aung et al. reported that the corrosion resistance of pure Mg/CNTs composite was reduced in comparison with the pure Mg in simulated sea water [30] and they also established that the corrosion resistance of pure Mg/CNT composite was weakened due to the galvanic corrosion between the Mg matrix and CNTs. However, they did not inspect the role of CNTs on the local corrosion behavior of the Mg matrix.

Further, it has been already reported that the improved corrosion performance of the CNT/AA 4032 alloy probably accompanied with the hydrophobic surface of alloy surface due to the addition of CNTs and further, CNTs integrated into AA 4032 alloy slow down the formation of oxide layer, resultant in a higher enhancement in surface protection

against corrosion [31]. It is understood that the improved corrosion resistance of the AA5083/MWCNT composite by Samuel Ratna Kumar et al. is mainly due to the strong interfacial bonding between the matrix alloy and reinforcement [32]. After immersion of investigated Mg alloy substrates in SBF, the naturally formed MgO film will convert into a film containing mostly of Mg(OH)<sub>2</sub>. The volume expansion from MgO to Mg(OH)<sub>2</sub> is attributed as the main disruption of the surface film and could explain the porous microstructure of the Mg(OH)<sub>2</sub> layer in the surface film. In the case of unreinforced, the formation of Mg(OH)<sub>2</sub> layer at the initial period of corrosion process performs as a physical barrier for the further degradation, but the existence of Cl<sup>-</sup> ruptured the Mg(OH)<sub>2</sub> layer by producing MgCl<sub>2</sub> crystals which further increase the formation of pits. Dissolution of MgCl<sub>2</sub> crystals further increases the degradation rate of the sample [33]. However, the addition of CNTs into Mg matrix improves the stability of Mg(OH)<sub>2</sub> layer by reinforcing it and inhibiting the dissolution from the attack of Cl ion from SBF. Turhan et al. also reported that the investigation of the corrosion product layers specifies that reinforcement of MWNTs in the matrix results to a more homogeneous surface coverage by corrosion products, and the lowest thickness of the corrosion product layer [34].

It is important to mention that the reinforcement of CNT does not always enhance the performance of the composite, on contrary may result in weakening the performance in other features [35]. The effect of corrosion probably also occur due to the manufacturing and further, processing techniques of MMCs may also direct to the development of an interphase between the reinforcement and matrix material. The weakest or the strongest part of particulate composite is the interface between the base alloy and the reinforcement.

Based on the obtained results, it can be concluded that the presence of CNTs improves the stability of the Mg(OH)<sub>2</sub> and efficiently regulate the degradation behavior in SBF. Surface characterization after immersion in SBF revealed the rapid formation of bone-like apatite layer on the surface, validated a good bioactivity of the AZ31 nanocomposite samples.

### 3.2 Invitro Mineralization During Immersion in SBF

To explore the invitro mineralization of unreinforced and CNT reinforced nanocomposite samples, the surface morphologies of after immersion in SBF for 3, 7, and 14 days are shown in Fig. 8. After 3 days of immersion, the unreinforced AZ31 samples corroded severely and many cracks found on its surface. Generally, the magnesium alloy surface reacts with water and change to Mg(OH)<sub>2</sub> film. Mg(OH)<sub>2</sub> associates with some H<sub>2</sub>O molecules to produce hydrate of Mg(OH)<sub>2</sub>·nH<sub>2</sub>O. While the surfaces are dried out, the film contracts because of dehydration hence creating many cracks [36]. With prolonging the exposure period to 7 days, the cracks on the nanocomposite surface were covered by a large quantity of Ca–P deposits on the surface.

Results obtained from EDS analysis are shown in Fig. 9. The weight percent of magnesium in the corrosion product of unreinforced AZ31 alloy was found to be increased after immersion, which further confirmed that sample surface was completely covered with Mg(OH)<sub>2</sub>. Conversely in the EDS spectrum of nanocomposite samples, a little amount of Ca/P mineral phase was observed, which indicate that the surface layer was rich in Mg, O, Ca and P. In the case of nanocomposite samples, the weight percent of magnesium in the corrosion product film after exposure for 4 and 7 days are considerably lesser than that after immersion for 1 day.

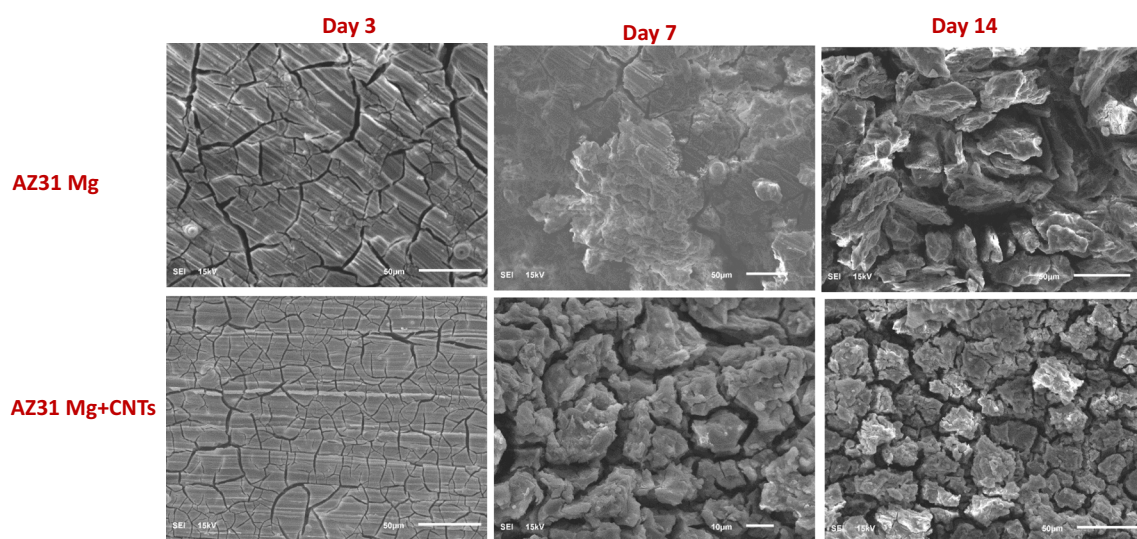


**Fig. 8** SEM results for unreinforced AZ31 and its reinforced nanocomposite samples after different period of immersion in SBF medium

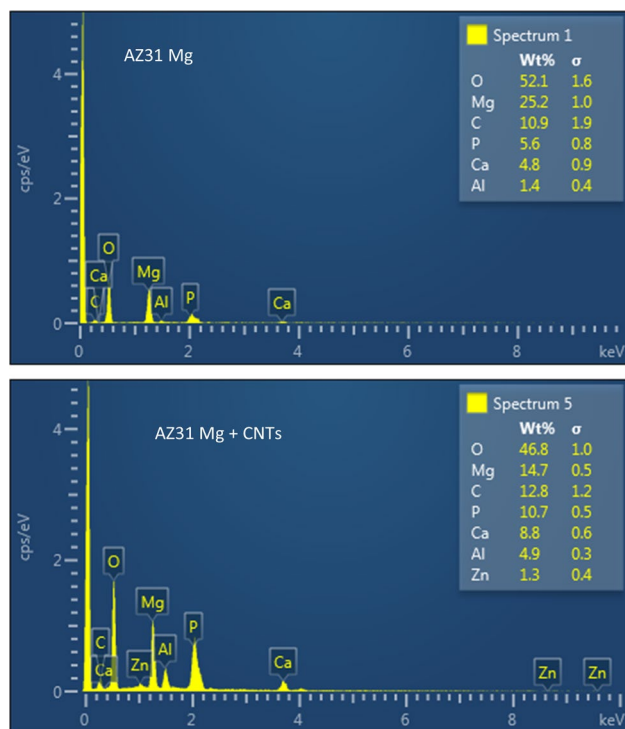


**Fig. 9** SEM results for unreinforced AZ31 and its reinforced nanocomposite samples after different period of immersion in SBF medium

However, the relatively higher weight percentage of P, O, and Ca suggests the accumulation of corrosion product layer with richer calcium phosphate compounds. Furthermore, the Ca/P ratio of the nanocomposite substrates after exposure for 1, 7, and 14 days was found to be 1.52, 1.60, and 1.71, respectively. The increase in the Ca/P ratio is generally accompanied with the conversion of dicalcium phosphate (DCPA) into hydroxyapatite (HA).

The FTIR spectra of unreinforced and nanocomposite samples on immersion in SBF after 14 days are shown in Fig. 10a. The broad absorption band appeared around 3400–3250  $\text{cm}^{-1}$  due to adsorbed  $\text{H}_2\text{O}$  on the surface and two broad bands at 2337 and 2446  $\text{cm}^{-1}$  for atmospheric  $\text{CO}_2$  were detected [37]. The peak at 567  $\text{cm}^{-1}$  results from the  $\nu_4$  mode of O–P–bending, whereas the peak observed at 1004  $\text{cm}^{-1}$  indicated the  $\nu_3$  band of P–O stretching mode. The peaks approximately at 1420 and 860  $\text{cm}^{-1}$  correspond to the  $\nu_3$  vibration mode of carbonate incorporated in the apatite. The absorption band at 1643  $\text{cm}^{-1}$  were ascribed to C–O of the  $\text{CO}_3$  group. The obtained result is in good agreement with previous reports of IR analysis of apatite [38, 39]. Based on above remarks, it could be corroborated that the apatite layer was formed on nanocomposite samples after immersion in SBF solution.

The formation of corrosion product layer with HA deposits on the surface of nanocomposite samples after exposure

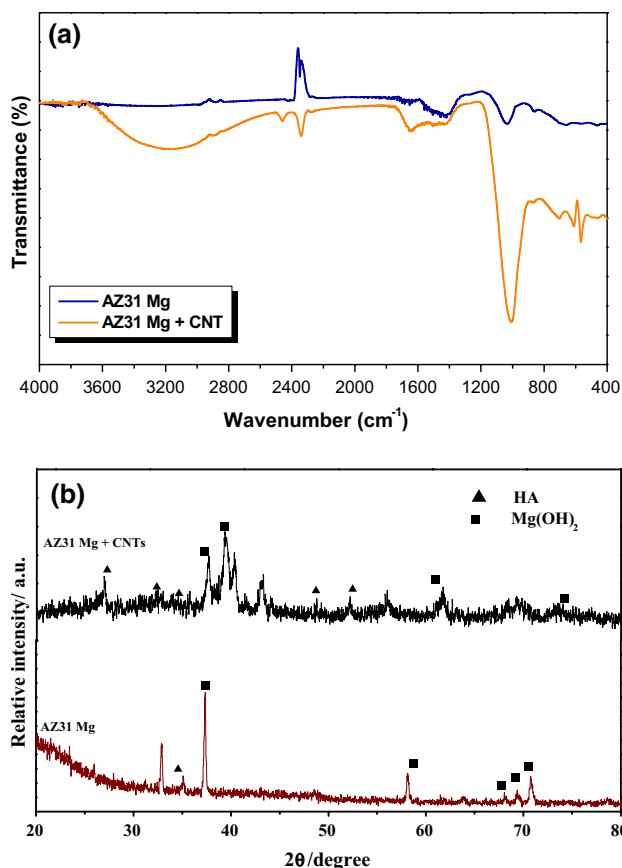


**Fig. 10** a ATR-IR and b XRD results for unreinforced AZ31 and its reinforced nanocomposite samples after immersion in SBF medium

in SBF was verified using XRD analysis. The XRD pattern of nanocomposite sample (Fig. 10b) displays the distinctive peaks of HA at 25.27°, 30.92°, 34.15°, 35.25°, 41.90°, 55.12°, 66.21° and 72.93°, which are corresponding to semi crystalline HA [40]. However, this HA peak was not identified in corrosion film produced in bare samples. Furthermore, the relative intensity of calcium phosphate compounds and  $\text{Mg}(\text{OH})_2$  were very weak in association with the intensity of Mg peak. Moreover, it could be noticed that the intensity of AZ31 alloy peaks reduced abruptly for nanocomposites, which probably ascribed to the pointedly increased thickness of the  $\text{Mg}(\text{OH})_2$  deposition and HA layer on the nanocomposite sample, implying that the addition of CNTs induced the excellent bioactivity. In essence, CNTs can favor the apatite precipitation after immersion in SBF and thus improve the bioactivity of Mg alloys.

### 3.3 Hydrogen Evolution Reaction Test

The collection of hydrogen gas is a precise corrosion/degradation test for magnesium alloys due to its low hydrogen evolution potential, which indicates that the cathodic

reaction of Mg is mostly hydrogen production rather than reducing dissolved oxygen [41]. Besides, the cathodic reaction is continuously dominated in the magnesium corrosion, hence the corrosion rate of magnesium alloy AZ31 is suitable to estimate by hydrogen evolution reactions. Deviation of hydrogen evolution with immersion time is presented in Fig. 11a. The unreinforced AZ31 and its CNT reinforced nanocomposite samples exhibited distinctively different corrosion rates during immersion in SBF medium. At the initial period of immersion, a prompt formation of hydrogen bubbles was noticed on the alloy surface due to the reaction of Mg with chlorides from SBF medium. After 48 h of immersion, the hydrogen evolution rate was slightly reduced. As expected, unreinforced samples exhibited a rapid and abundant amount of accumulative hydrogen with immersion time whereas CNT reinforced nanocomposite samples released relatively lesser volumes of hydrogen. After 336 h of immersion, the evolved hydrogen gas volume in the case of unreinforced AZ31 alloy was about  $4.5 \text{ ml/cm}^2$ , which reduced to less than half in volume (i.e.,  $2 \text{ ml/cm}^2$ ) in the case of CNT reinforced nanocomposite samples. In addition, the weight losses presented by the unreinforced and nanocomposite samples during the immersion in SBF for 336 h

were utilized to assess their corrosion resistance behavior, as can be understood in Fig. 11b.

In this study, the unreinforced AZ31 alloy samples showed the maximum weight loss of  $43.1 \pm 2.1 \text{ mg/cm}^2$  while the nanocomposite samples experienced the lowest weight loss of only  $29.1 \pm 1.3 \text{ mg/cm}^2$ . The results of hydrogen evolution and weight loss revealed that the corrosion resistance behavior of the AZ31 alloy was efficiently enhanced by the addition of CNTs as reinforcement. Figure 11c, d shows the photographic images of the unreinforced and nanocomposite samples after 14 days of immersion in SBF. By 14 days of immersion, both the samples had a significantly darker appearance and in particular, unreinforced samples showed clear edge effect with very large pores and loss of material, while the CNT reinforced nanocomposite samples appeared darkened but without obvious damage and material loss. In essence, it was proven that the enhancement of corrosion resistance performance was predominantly attributed to the formation of the protective layer with rapid mineralization, which hindered the aggressive ions arriving into the surface of the base substrate during immersion in SBF medium.

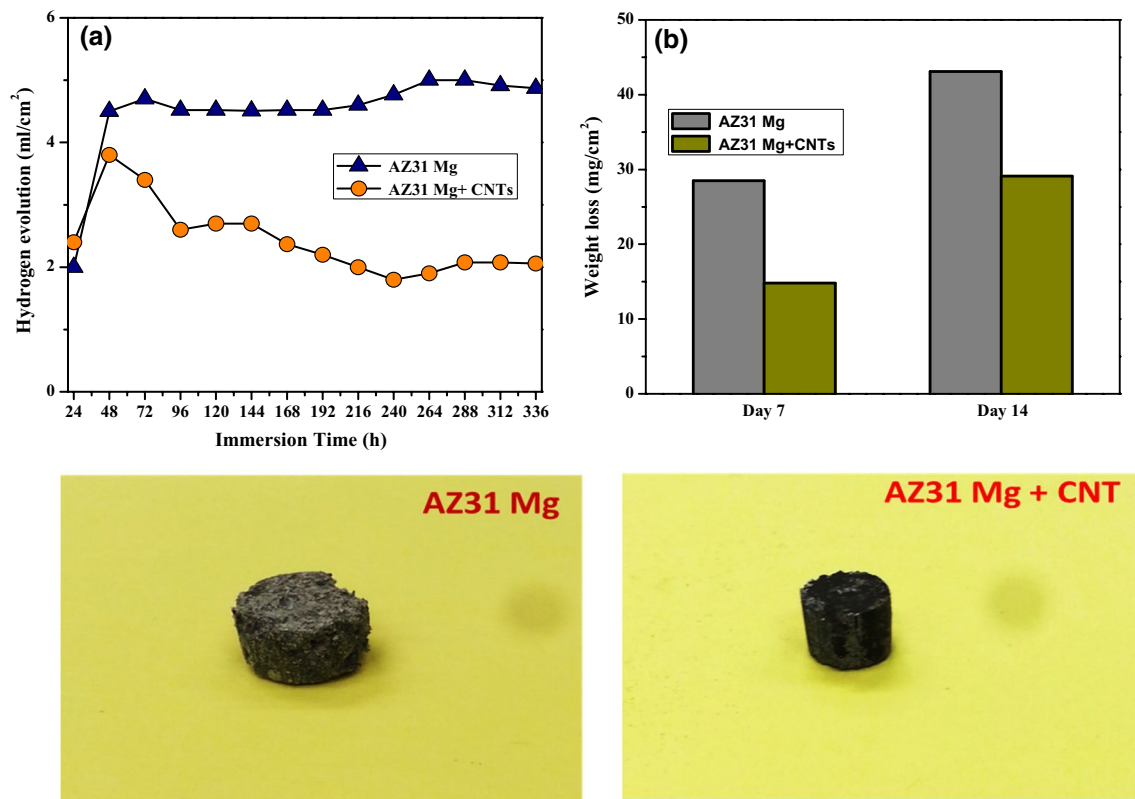


**Fig. 11** **a** Hydrogen evolution test results, **b** weight loss results and visual images of **c** AZ31 and **d** AZ31 nanocomposite samples after 14 days of immersion in SBF

## 4 Conclusions

In this study, systematic investigation of the electrochemical corrosion and degradation performances of AZ31 alloys with CNTs was done using electrochemical techniques, hydrogen evolution, and weight loss in SBF. In conclusion, CNTs reinforcement enhanced the corrosion resistant performance of AZ31 alloy which reflected in higher  $R_1$ ,  $R_2$  and considerably lower capacitive loop in short EIS test. The CNT reinforcement also reduced corrosion current densities and increased corrosion potential of the AZ31 alloy when tested for up to 336 h due to formation of CNT induced protective surface layer. Hydrogen evolution test suggested that the degradation behavior of AZ31 alloy was effectively improved after reinforced with CNTs. From the invitro biocompatibility test results, it could be concluded that the corrosion product layer contained an amorphous  $Mg(OH)_2$  and apatite like layer which can further increase the bioactivity of AZ31 alloy due to reinforcement with CNTs.

**Acknowledgements** The authors would like to acknowledge the support provided by the Deanship of Scientific Research (DSR) at King Fahd University of Petroleum and Minerals (KFUPM) for funding this work through Project No. IN151021.

## References

1. Y. Xiang, Z. Ning, M. Hua, C. Wang, F. Cui, *J. Mater. Chem. B* **1**, 4773 (2013)
2. L. Mao, L. Shen, J. Niu, J. Zhang, Y. Wenjiang Ding, R. Fan, G. Yuan, *Nanoscale* **5**, 9517 (2013)
3. S. Agarwal, J. Curtin, B. Duffy, S. Jaiswal, *Mater. Sci. Eng., C* **68**, 948 (2016)
4. X. Li, X. Liu, S. Wu, K.W.K. Yeung, Y. Zheng, P.K. Chu, *Acta Biomater.* **45**, 2 (2016)
5. T. Ishizaki, M. Okido, Y. Masuda, N. Saito, M. Sakamoto, *Langmuir* **27**, 6009 (2011)
6. H. Feng, X. Zhang, W. Guosong, W. Jin, Q. Hao, G. Wang, Y. Huang, P.K. Chu, *RSC Adv.* **6**, 14756 (2016)
7. A. Madhankumar, E. Thangavel, S. Ramakrishna, I.B. Obot, H.C. Jung, K.S. Shin, Z.M. Gasem, H. Kim, D.E. Kim, *RSC Adv.* **4**, 24272 (2014)
8. M. Paramsothy, S.F. Hassan, N. Srikanth, M. Gupta, *J. Nanosci. Nanotechnology* **10**, 956 (2010)
9. Y Shimizu, *In Tech, Croatia*, **491** (2011)
10. G.Q. Han, J.H. Shen, X.X. Ye, B. Chen, H. Imai, K. Kondoh, W.B. Du, *Mater. Lett.* **181**, 300 (2016)
11. A. Sabetghadam Isfahani, M. Abbasi, S.M.H. Sharifi, M. Fattahi, S. Amirkhanlou, Y. Fattahi, *Diamond Relat. Mater.* **69**, 160 (2016)
12. S. Kumar, R. Rani, N. Dilbaghi, K. Tankeshwar, K.H. Kim, *Chem. Soc. Rev.* **46**, 158 (2017)
13. R. Alshehri, A.M. Ilyas, A. Hasan, A. Arnaout, F. Ahmed, A. Memi, *J. Med. Chem.* **59**, 8149 (2016)
14. H. Byung-Dong, L. Jung-Min, P. Dong-Soo, C. Jong-Jin, R. Jungho, Y. Woon-Ha et al., *Acta Biomater.* **5**, 3205 (2009)
15. A. Dey, K.M. Pandey, *Adv. Mater. Sci.* **42**, 58 (2015)
16. A.Y. Adesina, Z.M. Gasem, A.M. Kumar, *Metall. Mater. Trans. B* **48B**, 1321 (2017)
17. Y. Ding, C. Wen, P. Hodgson, Y. Li, *J. Mater. Chem. B* **2**, 1912 (2014)
18. J. Li, B. Zhang, Q. Wei, N. Wang, B. Hou, *Electrochim. Acta* **238**, 156 (2017)
19. N.G. Wang, R.C. Wang, C.Q. Peng, Y. Feng, *J. Mater. Eng. Perform.* **21**, 1300 (2012)
20. M. Ascencio, M. Pegguleryuz, S. Omanovic, *Corros. Sci.* **87**, 489 (2014)
21. E. Ghali, W. Dietzel, K.U. Kainer, *J. Mater. Eng. Perform.* **13**, 517 (2004)
22. Y. Song, D. Shan, R. Chen, E.-H. Han, *Corros. Sci.* **51**, 1087 (2009)
23. N. Pebere, C. Riera, F. Dabosi, *Electrochim. Acta* **35**, 555 (1990)
24. P.G. Pawar, R. Xing, R.C. Kambale, A.M. Kumar, S. Liu, S.S. Latthe, *Prog. Org. Coat.* **105**, 235 (2017)
25. Y.C. Xin, *J. Mater. Res.* **22**, 2004 (2007)
26. A.M. Kumar, B. Suresh, S. Das, I.B. Obot, A.Y. Adesina, S. Ramakrishna, *Carbo. Poly.* **173**, 121 (2017)
27. G. Baril, G. Galicia, C. Deslouis, N. Pebere, B. Tribollet, V. Vivier, *J. Electrochem. Soc.* **154**, C108 (2007)
28. H. Mindivana, A. Efe, A.H. Kosatepe, E.S. Kayali, *Surf. Sci.* **318**, 234 (2014)
29. M. Endo, T. Hayashi, I. Itoh, Y.A. Kim, D. Shimamoto, H. Muramatsu, Y. Shimizu, S. Morimoto, M. Terrones, S. Iinou, S. Koide, *Appl. Phys. Lett.* **92**, 1 (2008)
30. N.N. Aung, W. Zhou, C.S. Goh, S.M.L. Nai, J. Wei, *Corros. Sci.* **52**, 1551 (2010)
31. M.S.S. Saravanan, S.P.K. Babu, K. Sivaprasad, *Exper. Techniq.* **38**, 48 (2014)
32. P.S.S.R. Kumar, D.S.R. Smart, S.J. Alexis, *J. Asian Ceram.* **5**, 71 (2017)
33. M.S. Uddin, C. Hall, P. Murphy, *Sci. Technol. Adv. Mater.* **16**, 53501 (2015)
34. M.C. Turhan, Q. Li, H. Jha, R.F. Singer, S. Virtanen, *Electrochim. Acta* **56**, 7141 (2011)
35. N. Saikrishna, G.P.K. Reddy, B. Munirathinam, R. Dumpala, M. Jagannatham, B.R. Sunil, *J. Mag. Alloys* **6**, 1 (2011)
36. J. Zhang, X. Chi, Y. Jing, S. Lv, S. Liu, D. Fang, J.P. Zhuang, M. Zhang, R. Wu, *Sci. Rep.* **5**, 13933 (2015)
37. A. Madhankumar, N. Rajendran, *Ceram. Int.* **39**, 5639 (2013)
38. A. Madhankumar, N. Rajendran, *Surf. Coating Technol.* **213**, 155 (2012)
39. M. Karthega, S. Nagarajan, N. Rajendran, *Electrochimica Acta* **55**, 2201 (2010)
40. Y. Sasikumar, N. Rajendran, *Mater. Chem. Phys.* **138**, 114 (2013)
41. P. Tian, X. Demin, X. Liu, *Colloids Surf. B Bio Interfaces* **141**, 327 (2016)